Journal of Oceanology and Limnology
Vol. 40 No. 2, P. 438-455, 2022
https://doi.org/10.1007/s00343-021-0453-y

Tidal currents in the coastal waters east of Hainan Island in winter*

Min LI[1, 2, 3], Lingling XIE[1, 2, 3, **], Xiaolong ZONG[4], Junyi LI[1, 2 ,3], Mingming LI[1, 2, 3], Tong YAN[5, 6], Ronglei HAN[7]

[1] *Laboratory for Coastal Ocean Variation and Disaster Prediction, Guangdong Ocean University, Zhanjiang 524088, China*

[2] *Key Laboratory of Climate, Resources and Environment in Continental Shelf Sea and Deep Sea of Department of Education of Guangdong Province, Guangdong Ocean University, Zhanjiang 524088, China*

[3] *Marine Resources Big Data Center of South China Sea, Southern Marine Science and Engineering Guangdong Laboratory (Zhanjiang), Zhanjiang 524013, China*

[4] *Institute of Marine Sciences, Shantou University, Shantou 515063, China*

[5] *South China Sea Institute of Oceanology, Chinese Academy of Sciences, Guangzhou 510301, China*

[6] *Southern Marine Science and Engineering Guangdong Laboratory (Guangzhou), Guangzhou 511458, China*

[7] *Key Laboratory of Space Laser Communication and Detection Technology, Shanghai Institute of Optics and Fine Mechanics, Chinese Academy of Sciences, Shanghai 201800, China*

Received Nov. 24, 2020; accepted in principle Jan. 31, 2021; accepted for publication Apr. 1, 2021

Abstract Using the 25-h continuing hydrographic observations at three successive stations in February 2012 and the mooring time series of current observations from January to March 2015, the tidal currents and tidal energy fluxes in the coastal waters east of Hainan Island in the northwestern South China Sea were analyzed. The diurnal and semidiurnal (using K_1 and M_2 as proxies, respectively) tidal currents and associated isopycnal undulations were derived with harmonic analysis. Results show that the velocities of the diurnal and semidiurnal tides derived from the 25-h observations are comparable to those from the mooring series. The semi-major axes of the tidal ellipses were *O*(4–7 cm/s) for barotropic tides and *O*(2–4 cm/s) for baroclinic tides. The directions were in NE–SW at deeper stations to N–S at the shallowest station for the diurnal tide and from NW–SE to NE–SW for the semidiurnal tide. Both the diurnal and semidiurnal isopycnal fluctuations reached *O*(5 m), *O*(8 m), and *O*(10 m) at the cross-shelf stations (H03, H04, and H05) from 35 m, 45 m, to 55 m, respectively, showing insignificant vertical variation, and the barotropic signals were predominate. The baroclinic diurnal tide showed first-mode structures at H03-05, as does the semidiurnal tide at H03. The semidiurnal tide at H04 and H05 exhibited higher-mode structures. The time series of both the alongshore and cross-shore components reveal the vertically propagation features of the baroclinic tidal phase and energy. The calculated horizontal energy fluxes of the diurnal and semidiurnal internal tides decreased from *O*(0.1 W/m) at H05 to *O*(0.01 W/m) at H03, implying a propagation and dissipation of energy from offshore to inshore.

Keyword: tidal current; barotropic tide; internal tide; energy flux; east of Hainan Island

1 INTRODUCTION

Tidal currents, as a type of intrinsic motion and an important dynamic process in the ocean, play an important role in ocean circulation, mixing, and the ocean ecosystem (Munk and Wunsch, 1998; Egbert and Ray, 2000). Improving the understanding of tidal motions and related mechanisms, especially the tidal features in coastal regions, is crucial to engineering

* Supported by the National Nature Science Foundation of China (Nos. 41776034, 41506018, 41706025, 41706129), the First-Class Discipline Plan of Guangdong Province (Nos. CYL231419012, 231819002), the Matched Grant of Guangdong Ocean University (No. P15299), the PhD Start-up Grant of Guangdong Ocean University (No. R20022), the Project of Enhancing School with Innovation of Guangdong University (No. Q16303), the Project of Enhancing School with Innovation of Education Department of Guangdong Province (Nos. 2018KQNCX082, 2019KCXTF021), and the Southern Marine Science and Engineering Guangdong Laboratory (Guangzhou) (No. GML2019ZD0303)
** Corresponding author: xiell@gdou.edu.cn

projects, fishery production, and economic activities. The region east of Hainan Island (often called Qiongdong, the east of Hainan Island) is on the northwestern South China Sea (SCS) shelf and slope, with a rather flat topography near the coast and a steep continental slope offshore. The isobaths in this area are nearly parallel to the coastline in the northeast-southwest (NE-SW) direction. The shoaling features and existence of seasonal upwelling/downwelling near the coast (Xie et al., 2012; Hu and Wang, 2016; Xie et al., 2017) provide a complex dynamical environment for tidal currents, as well as the propagation and possible local production of internal tides.

Some early studies in the 1980s depicted the properties of the tidal current east of Hainan Island using model simulation. Ye and Robinson (1983) used a two-dimensional hydrodynamic model to show that the velocities of both the K_1 and M_2 tidal currents are less than 5 cm/s east of the island and approximately 5–10 cm/s in the northeast. Ding (1986) showed that the major axes of both the K_1 and M_2 tidal current ellipses are parallel to the isobaths in the north and are aligned across the isobaths in the south. The vector of the K_1 tide rotates clockwise, while that of the M_2 tide rotates anticlockwise. Fang (1986) combined simulation and observation to provide the cotidal chart and distribution of the velocity maxima of the K_1 and M_2 tides around Hainan Island. The results showed that the maximum velocity of the K_1 tide was approximately 10 cm/s in the east and more than 20 cm/s in the northeast; meanwhile, that of the M_2 tide is 10 m/s in the east and between 10 and 20 cm/s in the northeast. Cao and Fang (1990) and Fang et al. (1994) used the mean of K_1 and O_1 to represent the diurnal tide and showed the cotidal chart and tidal currents of the diurnal tide and M_2 tide, revealing that the major axes of the diurnal tidal ellipses in the east of Hainan Island are mainly in the NW-SE direction, while those of the M_2 tidal ellipses are nearly in the N-S direction. Fang et al. (1999) simulated the four principal tidal constituents and showed that the tide in the SCS is preserved by the tidal energy flux from the Luzon Strait. Zu et al. (2008) analyzed the tides and dynamic processes in the SCS using a barotropic tide model in which the altimetry data were assimilated. Zhu (2009) and Yang et al. (2013) used the finite-volume coastal ocean model to simulate the tide and tidal currents in the northern SCS and China seas, respectively. Gao (2013) showed the tidal ellipses of the four primary constituents in the entire SCS using the adjoint assimilation method. The model simulations concentrated either on large domains with robust results in the shallow shelf region, or on specific regions in deep water, the tide condition on the shallow shelf east of Hainan Island remains uncertain.

Regarding the observational analysis of the tidal current east of Hainan Island, one of the areas east of Hainan Island that has received attention in the literature is the offshore region of Wenchang (Ke, 2007; Xu et al., 2011; He et al., 2012). Analysis of mooring data for approximately six months at a station deeper than 100 m offshore Wenchang showed that the diurnal internal tide is prominent with semidiurnal internal tides arising intermittently (Ke, 2007). Xu et al. (2011) analyzed a two-month time series obtained from the Acoustic Doppler Current Profiler (ADCP) offshore the Wenchang station and found that the M_2 tide is the dominant barotropic tidal constituent. Although the diurnal tide was found to be mainly a first-mode tide, the semidiurnal tide exhibited a higher modal structure. However, He et al. (2012) showed that the clockwise O_1 tide is dominant east of Wenchang using a year-long time series at the surface layer. The velocities of the clockwise-rotating K_1 and anticlockwise-rotating M_2 are both weak (less than 2 cm/s). They also found that the tide type is mainly irregular diurnal on the northern shelf and slope and becomes diurnal in the deep region. The region near Xisha Island is also a research hotspot. Deng et al. (2013) analyzed a 21-d velocity time series obtained on the shelf near Xisha Island in July and found that the barotropic tide was dominant and the baroclinic tide was weak. The barotropic tide is mainly the K_1 tide, followed by the O_1 tide, both of which have clockwise-rotating ellipses. Yan et al. (2016) investigated the features of the tides northwest of Xisha Island using a five-year moored time series; their results revealed that the diurnal signals were dominant in both the barotropic and baroclinic tides. The barotropic velocity vectors of the four main constituents rotate clockwise except for that of the M_2 tide. The baroclinic K_1 tide appears to exhibit a semi-annual variation with stronger signals in the summer and winter. Yan et al. (2020) presented the tidal ellipses of four principal constituents from moored time series in the northeast, southeast, and south of the Hainan Island approximately along the 50-m isobath. The results showed that the major axes of all the four constituents in the northeast are nearly in the N-S direction and the maximum velocity of the

semidiurnal tide is 14.4 cm/s, which is about twice that of the diurnal tide. The ellipses in the southeast and south are approximately along the isobaths and the velocity of the diurnal tide is stronger than that of the semidiurnal tide.

Studies on the tidal current east of Hainan Island show limitations in the nearshore region. Particularly, intensive observations are rare to reveal the cross-shelf variation of the tidal current on the shallow shelf. Moreover, previous studies have shown that the tide type east of Hainan Island is complicated, and it is the transition region of two tide/tidal current types, irregular semidiurnal tide/tidal current and irregular diurnal tide/tidal current (Editorial Board of Marine Atlas, 2006; Yan et al., 2020). Therefore, more works are necessary to sharpen our view of the tidal current in this region. In this study, we focus on the properties and variation of the tidal current using data obtained from three successive stations northeast of Hainan Island (offshore Bo'ao city) and a two-month moored time series from a seabed-based platform southeast of the island (offshore Wanning city). Section 2 introduces the data and methods used in this study and Section 3 provides background fields, such as hydrography and wind, the properties of the barotropic tides, and the features and energy flux of the internal tides, as well as their effects on the isopycnal fluctuations. Discussion and conclusion are provided in Section 4 and Section 5, respectively.

2 MATERIAL AND METHOD

2.1 Successive observation at three stations

During the cruise investigation in the winter of 2012, three successive stations (H03–05, Fig.1) across the shelf northeast of Hainan Island were implemented from 15:58 (local time), February 23 to 17:39 (local time), February 24. The depths of the three stations are 34 m (H03), 44 m (H04), and 54 m (H05), respectively, and the distance between two adjacent stations is 4.3 km. The observation order is H03-H04-H05, which means the observation was repeated beginning at H03 after finishing at H05. Current and hydrographic profiles were obtained from shipboard 300-kHz ADCP and a conductivity-temperature-depth (CTD) profiler approximately every three hours at each station, resulting in nine observations for each station. The ADCP was set up at the side of the ship and maintained at 6-m depth. The depth bin was 4 m and the sampling interval was 30 s.

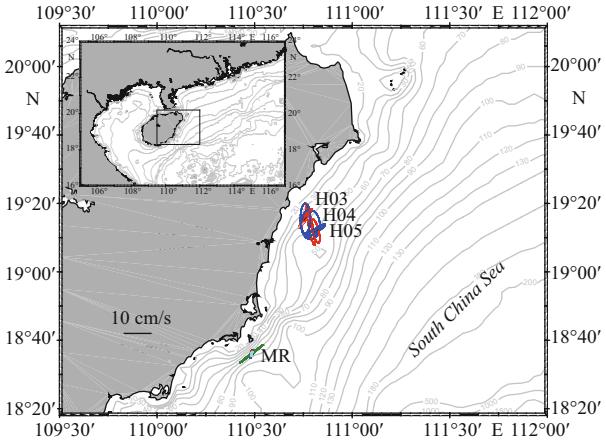

Fig.1 Bathymetry of northern South China Sea and zoomed-in study domain based on ETOPOv2 global topography

Showing barotropic tidal ellipses (blue: K_1; red: M_2; green: O_1; cyan: S_2) at each site using the scale at the lower left. The locations of the three successive stations (H03–05) and the mooring (MR) are marked. The properties of the ellipses are shown in Table 1. The gray lines denote isobaths.

2.2 Mooring time series offshore of Wanning

A seabed-based monitoring platform system with an upward-looking ADCP was deployed offshore of Wanning, Hainan (18°36′N, 110°29′E) from January 6 to March 3, 2015 (MR, Fig.1). The data depths ranged from 4 m to 78 m, with temporal and vertical resolutions of 10 min and 2 m, respectively. The data were used to present the tidal current southeast of Hainan Island. Unfortunately, the hydrography or stratification information is unknown because there is no hydrographic sensor on the platform.

2.3 Methodology

To qualify the tidal current, the least square method is applied to extract the diurnal and semidiurnal tides from the barotropic and baroclinic currents at the three successive stations. Previous studies revealed that lunisolar tide (K_1, period: 23.94 h) and principal lunar tide (M_2, period: 12.42 h) are two primary tidal components northeast of Hainan Island (Fang, 1986). Note that the time series used here is not long enough to distinguish between the K_1 and O_1 tides or between the M_2 and S_2 tides. Therefore, we mainly focus on two major constituents, K_1 and M_2, for the successive stations.

The vertically averaged current is regarded as the barotropic current:

$$\overline{u_{\mathrm{bt}}}(t_i)=\frac{1}{H}\int u(z_h,t_i)\,\mathrm{d}z_h, \tag{1}$$

where H denotes the depth of the data and the subscript "bt" means barotropic. The barotropic current is regarded as the sum of the barotropic K_1 and M_2 tidal currents and the residual,

$$\begin{aligned}\overline{u_{\rm bt}}(t_i) &= u_{\rm bt}^0 + u_{\rm bt}^{\rm m}(t_i) + u_{\rm bt}^{\rm k}(t_i)\\ &= u_{\rm bt}^0 + \sum_{j=1}^{2} A_{\rm bt}^j \cdot \cos\left(\omega_{\rm bt}^j t_i - \phi_{\rm bt}^j\right)\\ i &= 1,2,3,\cdots,9,\end{aligned} \tag{2}$$

where superscripts "m", "k", and "0" denote M_2, K_1, and the residual, respectively. Subscript i=1, 2, 3, ···, 9 refers to the nine realizations at each station. $A_{\rm bt}^j$, $\omega_{\rm bt}^j$, $\varphi_{\rm bt}^j$, and t are the amplitude, frequency, initial phase, and local time, respectively. Using this formula and the least square method, the amplitudes and initial phases of the barotropic K_1 and M_2 tidal constituents were obtained. This traditional quasi-harmonic analysis method is usually used for tidal analysis with limited data and previous studies have indicated its effectiveness (Zhu et al., 2014; Gao et al., 2020).

The baroclinic current is computed by removing the barotropic current from the original time series:

$$u_{\rm bc}(z_h,t_i) = u(z_h,t_i) - \overline{u_{bt}}(t_i). \tag{3}$$

Similarly, the baroclinic current can be written as

$$\begin{aligned}u_{\rm bc}(z_h,t_i) &= u_{\rm bc}^0(z_h) + u_{\rm bc}^{\rm m}(z_h,t_i) + u_{\rm bc}^{\rm k}(z_h,t_i)\\ &= u_{\rm bc}^0 + \sum_{j=1}^{2} A_{\rm bc}^j \cdot \cos\left(\omega_{\rm bc}^j t_j - \phi_{\rm bc}^j\right),\\ i &= 1,2,3,\cdots,9,\end{aligned} \tag{4}$$

where subscript "bc" means baroclinic. The amplitudes and initial phases of the baroclinic K_1 and M_2 tidal currents were obtained using the same method and process.

Regarding the mooring data, the depth-average method is also used to obtain barotropic and baroclinic signals. The T-Tide harmonic analysis toolbox (Pawlowicz et al., 2002) was applied to the barotropic and baroclinic time series to extract the four major tidal components.

3 RESULT

3.1 Background field

3.1.1 Hydrography

The difference in potential temperatures at the upper and lower layers is approximately 1 °C at both H03 and H04 and approximately 2 °C at H05 (Fig.2a–c). The depth of the thermocline is ~20 m at the two shallow stations and approximately 10 m deeper at the deep station. The isotherms reveal prominent rises and falls with time at the three stations (Fig.2a–c), with a gradually decreasing amplitude from H05 to H03 (i.e., from offshore to inshore). Unlike the temperature, the vertical gradient of salinity increases from offshore to inshore. At H03 and H05, the isohalines show periodic fluctuations (Fig.2d & f), a situation similar to the isotherm variation, although the salinity was uniform during the observation at H05 (variation below 0.1). The stratification is strong at almost all depths at H03 and H04, especially at 10–20 m (Fig.2g & h). At H05, there are two patches with low stratification of approximately 10^{-6}/s^2 (Fig.2i), 18:00–00:00 below 30 m and 00:00–06:00 above 20 m, likely resulting from the enhanced mixing induced by the tidal and wind forcing, respectively.

3.1.2 Current

To investigate the current features related to the bottom topography, a new coordinate system is defined in which the x-axis is across the shore (139°T) and the y-axis is along the shore (49°T) with positive directions corresponding to the southeastward and northeastward directions, respectively. Note that the section was designed to be nearly perpendicular to the isobaths.

The barotropic current is dominant in the raw velocity field, which is shown as a strongly consistent feature with depth in Fig.3. The velocity maximum at H03 is approximately 10 cm/s and the currents are stronger at H04 and H05, reaching ~20 cm/s. The current in the cross-shore direction is prominently strong at H05, exhibiting a strong northwestward flow. The cross-shore velocity components at H03–05 are comparable to the along-shore components. The wind forcing is usually regarded as an important influence factor of the current structure and variability on the shallow continental shelf, which can also be seen later in Section 3.1.3. The cross-shore velocities at H03 reveal diurnal signal (Fig.3a), while the other scenarios of the velocities present remarkable semidiurnal signals (Fig.3b–f). Using the method mentioned above, the barotropic and baroclinic currents at all stations were computed (Fig.4). The velocity maxima of both the barotropic and baroclinic currents at H03 and H04 are ~10 cm/s and ~12 cm/s at H05. In addition, the percentages of barotropic current in the original current are calculated (numbers at the upper left of Fig.4a–c). The barotropic currents at all three stations present a periodic variation that is

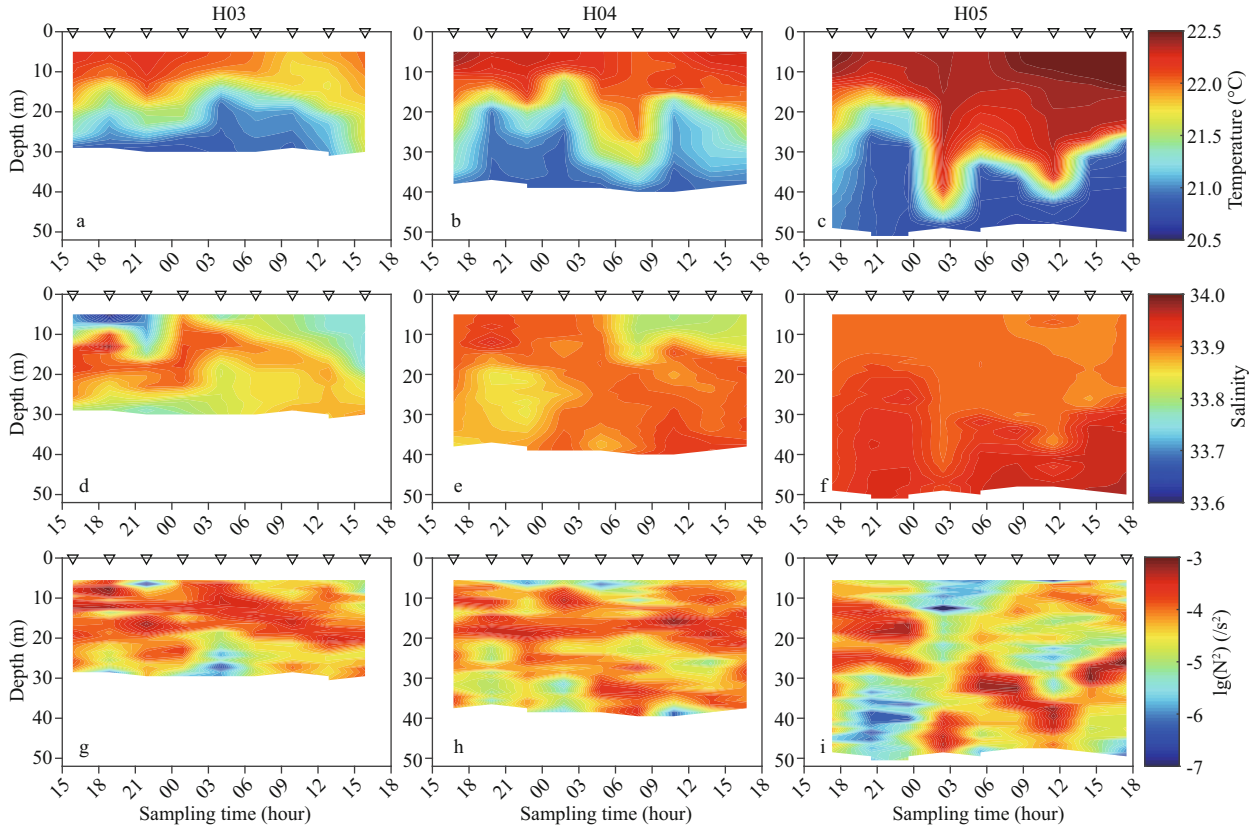

Fig.2 Potential temperature (a–c), salinity (d–f), and buoyancy frequency (g–i) at H03–05

The scales are shown at the right. The triangles denote the sampling time (local time).

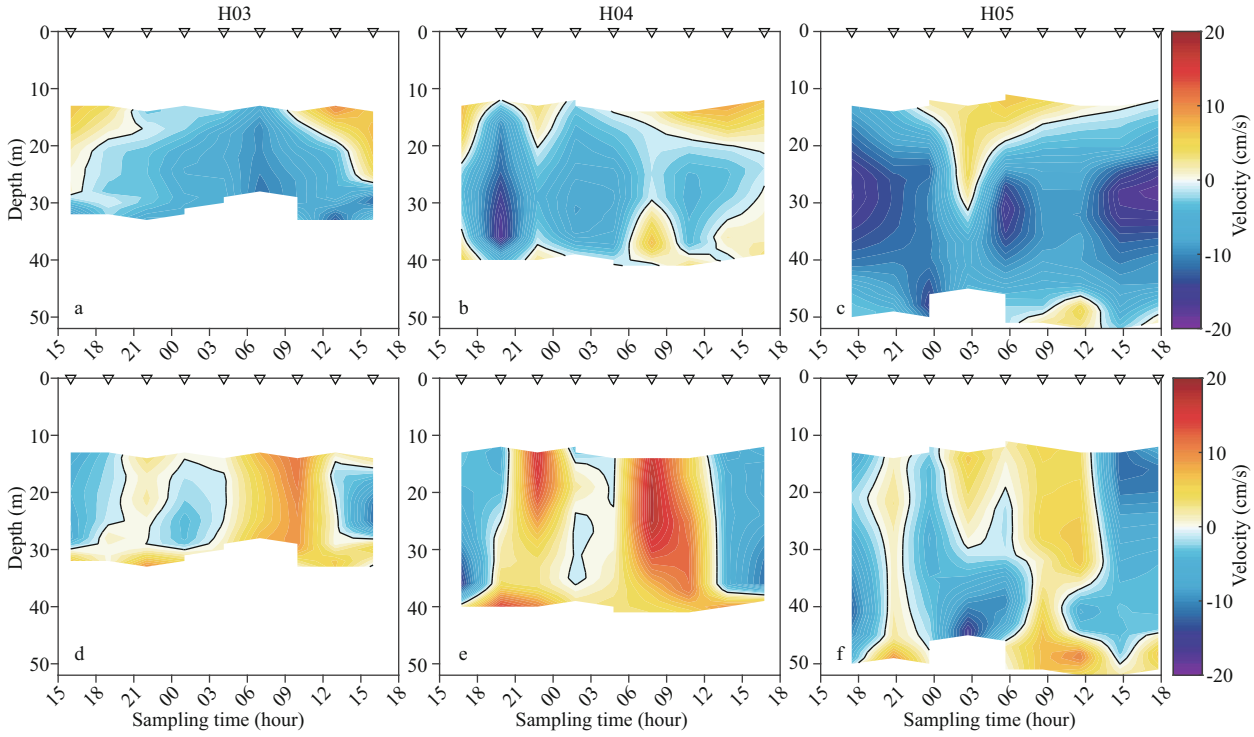

Fig.3 Variation of the raw current at three successive stations

The upper panel is the cross-shore components and the lower panel are the along-shore components. The triangles denote the sampling time. The black lines denote zero.

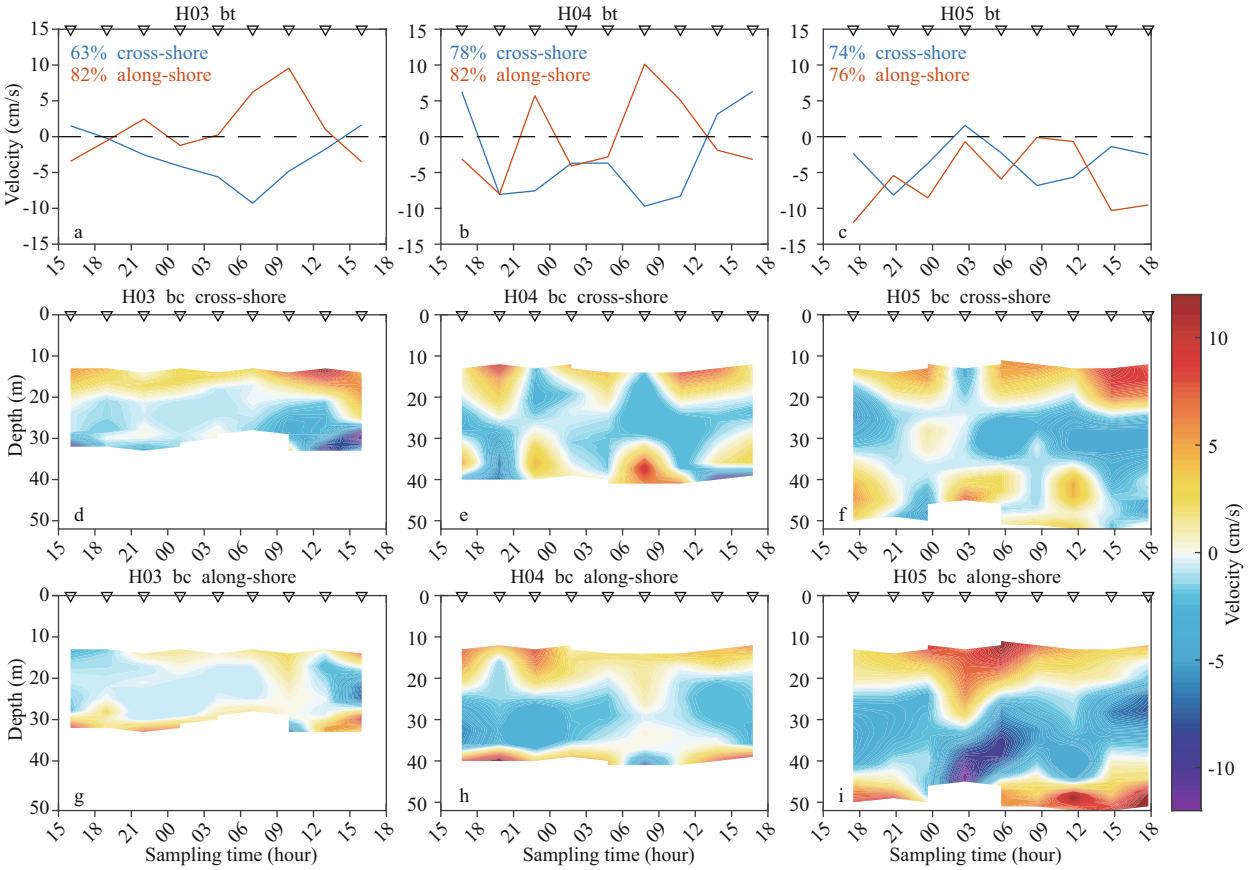

Fig.4 Barotropic velocities (a–c) and baroclinic velocities in cross-shore (d–f) and along-shore (g–i) directions at H03–05

The blue and red numbers in (a–c) denote the percentages of barotropic current in the raw current. The bt and bc denote barotropic and baroclinic, respectively.

possibly caused by diurnal or semidiurnal signals, occupying a rather large portion (more than 60%) of the original current. The cross-shore baroclinic current at H03 displays a two-layer structure during the observation, while the along-shore component at H03 and both components at H04–05 present a high-mode structure.

The residual currents are obtained from the decomposition in Section 2.3. The total residual mainly flows northeastward in the upper layer above 17 m and northwestward underneath at H03–04 (Fig.5). At H05, the current is weak above 20 m and strong westward underneath with a speed of greater than 10 cm/s. The barotropic residual flows northwestward at H03–04 at a speed of 4 cm/s and southwestward at H05 with a slightly stronger speed of 6 cm/s. The baroclinic currents at all three stations are more likely shoreward below 20 m, with speeds changing from 5 cm/s (offshore) to 2 cm/s (inshore) and flow offshore above. The westward/northwestward flow probably results from southerly and southeasterly wind forcing during a wind shift event (see Section 3.1.3).

The difference of velocity profiles at H03–05 is regarded as the combined effect from the shoaling

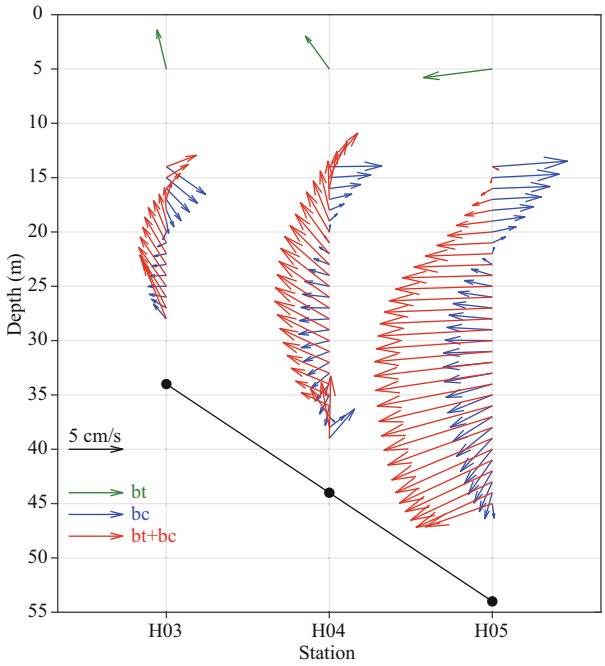

Fig.5 Residual current obtained from the least-squares method at H03–05

The green, blue, and red arrows denote barotropic (bt), baroclinic (bc), and entire residual currents (bt+bc), respectively. The black dots denote the observed bottom depth at H03–05.

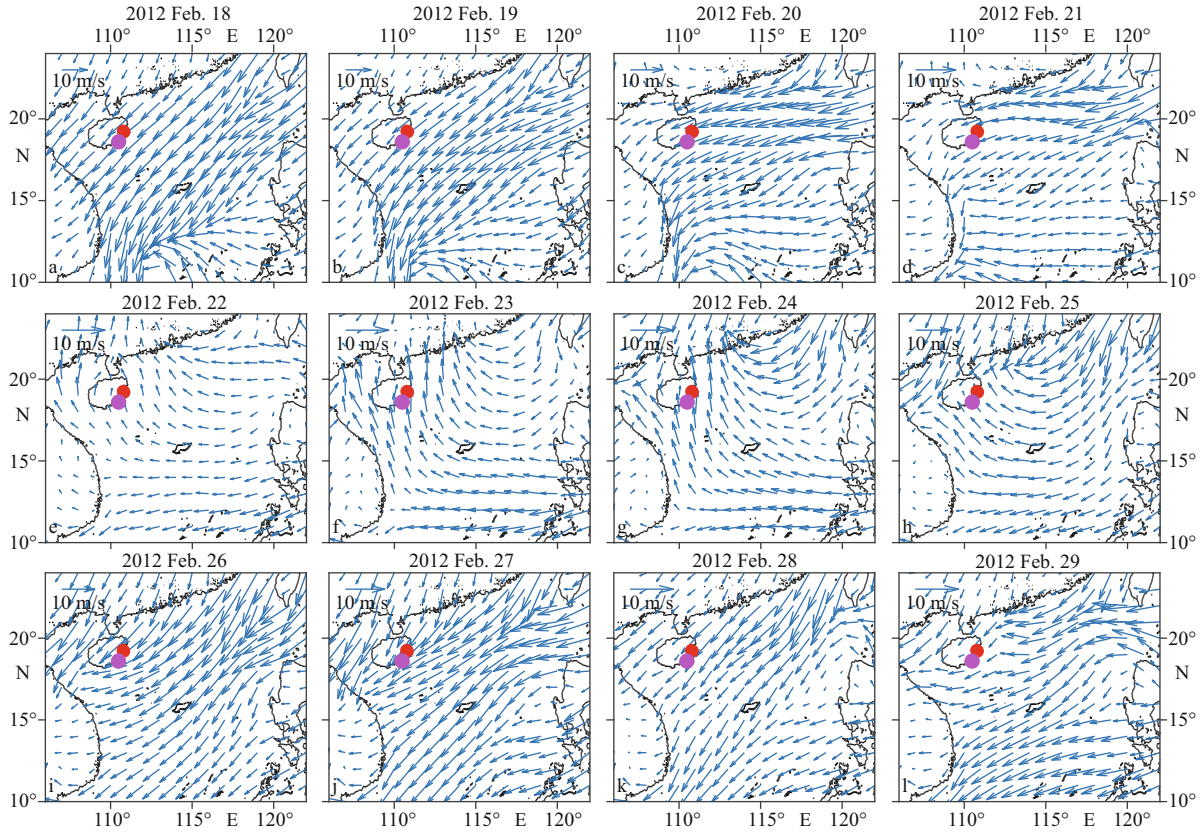

Fig.6 Wind field from Feb. 18 to 29 using the scale at the upper left of each figure part

The red and magenta dots denote the locations of the successive stations and mooring, respectively, and the successive observations were taken on February 23–24.

bottom topography at H03–05. The observed bottom depth is added at the three stations in Fig.5. One can see that a remarkable bottom slope exists at the section. The westward barotropic current at H05 tends to veer to the northwest when it flows from H05 to H03 with shoaling depths, following the potential vorticity conservation. The baroclinic currents at three stations reveal similar vertical structure, with a reversal at about 20 m, suggesting the mass balance between the shoreward current and the offshore current near the coastal boundary. In addition, cruise observations on the entire H-section with twelve stations (H01–12) from the inshore to the offshore shows remarkable temperature and salinity fronts at H03–05 (unpublished data), which might affect the baroclinic current as well. The dynamics, however, needs more investigation with support of observations on adjacent sections, which might be out of the scope of this study.

3.1.3 Wind field

Generally, the current variability on the shallow continental shelf is affected by local wind forcing. The northeasterly wind is climatically dominant in the SCS in winter, just as the wind field on February 18–19 (Fig.6). Notably, a wind shift event occurred on February 20, in which the wind veered first into the easterly wind and then into southerly and southeasterly winds over the following five days, during which observations were taken at the three successive stations (February 23–24). The wind speed decreased from 10 m/s before the event to less than 5 m/s afterward. The residual currents at H03, H04, and the upper layer of H05 are shown to be northwestward or westward (Fig.5), which is regarded to be affected by the shift in the wind. The wind data used here are from the European Center for Medium-Range Weather Forecast, six-hourly data with a spatial resolution of 0.125°.

3.2 Barotropic tide

The barotropic tidal current ellipses of K_1 and M_2 at the successive stations were obtained using the method described in Section 2.3 and are shown in Fig.1. The ellipse properties are listed in Table 1. The semimajor axis (or velocity maximum) of both barotropic K_1 and M_2 tides is approximately 2–5 cm/s, which is consistent with the results of Ye and Robinson (1983). For the K_1 tide, the major axis is in the NE-

Table 1 Ellipse properties of major diurnal and semidiurnal barotropic tidal constituents

Constituent	Station	Semi-major axis (cm/s)	Semi-minor axis (cm/s)	Inclination	Eccentricity	Phase
K_1	H03	5.40	1.75	89.83°	-0.32	219.76°
	H04	5.29	3.35	91.45°	-0.63	207.90°
	H05	4.14	0.69	34.33°	0.17	220.18°
	MR	1.62	0.08	72.24°	0.05	220.35°
M_2	H03	4.19	0.45	56.75°	-0.11	144.88°
	H04	7.40	0.73	100.98°	-0.10	153.17°
	H05	4.41	1.12	104.25°	-0.25	151.86°
	MR	1.32	0.19	80.38°	0.14	205.07°
O_1	MR	5.12	0.17	37.77°	-0.03	32.78°
S_2	MR	0.68	0.10	75.98°	-0.15	263.65°

Inclination refers to the angle that the major axis makes with the east direction, rotated anticlockwise. The positive/negative eccentricity denotes the velocity vector rotated anticlockwise/clockwise.

SW direction offshore (at H05 and MR) and aligns in the N-S direction onshore (at H03–04). The velocity vectors rotate clockwise at H03 and H04 and rotate anticlockwise at H05 and the MR site. The direction of the major axis of the K_1 tide is consistent with the result in Yan et al. (2020), while the rotation is opposite. With regard to the M_2 constituent, the direction of the major axis changes from NW-SE offshore (at H04–05) to NE-SW onshore (at H03) in the north; it is the same direction as the K_1 tide at the MR site. The vectors rotate clockwise at the three successive stations but anticlockwise at the MR site. The major axis is close to the direction of the isobaths at H03 but becomes more cross-shore at H04 and H05. The maxima of the K_1 and M_2 tidal currents are comparable at each station, although the currents are stronger at the northern sites H03–05 (4–8 cm/s) than that at the southern site MR (1–2 cm/s), where there is a prominently strong O_1 tidal constituent (approximately 5 cm/s) with a rectilinear ellipse parallel to the isobaths.

The tide type is characterized by the tidal type number (TN), which is defined as the sum of the amplitudes of the major diurnal tides divided by the sum of the amplitudes of the major semidiurnal tides. The tide type is regarded as regular semidiurnal tide when the TN is less than 0.5, irregular semidiurnal tide when the TN is between 0.5 and 2, irregular diurnal tide when the TN is between 2 and 4, and regular diurnal tide when the TN is greater than 4. The tidal type numbers at H03–05 and MR are 1.3, 0.7, 0.9, and 3.4, respectively, suggesting that the tidal current east of Hainan Island is mixed tide with irregular semidiurnal tide at H03–05 and irregular diurnal tide at the MR site.

For the results at the MR site, it is regarded to present the main features at the MR site since the two-month time series is long enough to identify them. For the results at the successive stations, the authors do not have long time series to check the persistence of the feature, which is a pity. Nevertheless, the results of barotropic tidal ellipses are compared with previous numerical and observational studies. It is revealed that the maximum velocity of M_2 tide at the successive stations is consistent with previous numerical result (~5 cm/s) near this area in Fang et al. (1999). Furthermore, the tide type of mixed tide with irregular semidiurnal tide at H03–05 is consistent with the results in Editorial Board of Marine Atlas (2006).

3.3 Internal tide

3.3.1 Primary property

The tidal ellipses of the diurnal (K_1) and semidiurnal (M_2) constituents derived from the baroclinic currents at H03–05 observed in February 2012 are shown in Fig.7. Similar to the barotropic tides, the amplitudes of the two baroclinic tidal constituents are comparable (2–4 cm/s), which is different from that in the northeastern continental shelf of the SCS, where the baroclinic K_1 tide is stronger than the M_2 tide (Gao et al., 2017). The K_1 tide shows a first-mode structure at the three stations, as does the M_2 tide at H03, as there is only one current reversal in the vertical. The transition depth is approximately 20 m at H03 and H04, and about 33 m at H05. However, the M_2 tide at H04 and H05 reveals a higher-mode structure with the transition depths of 26 m and 38 m at H04, and 24 m and 42 m at H05. Higher-mode structure of baroclinic tide in the northwestern South China Sea was previously reported in Xu et al. (2011). They showed

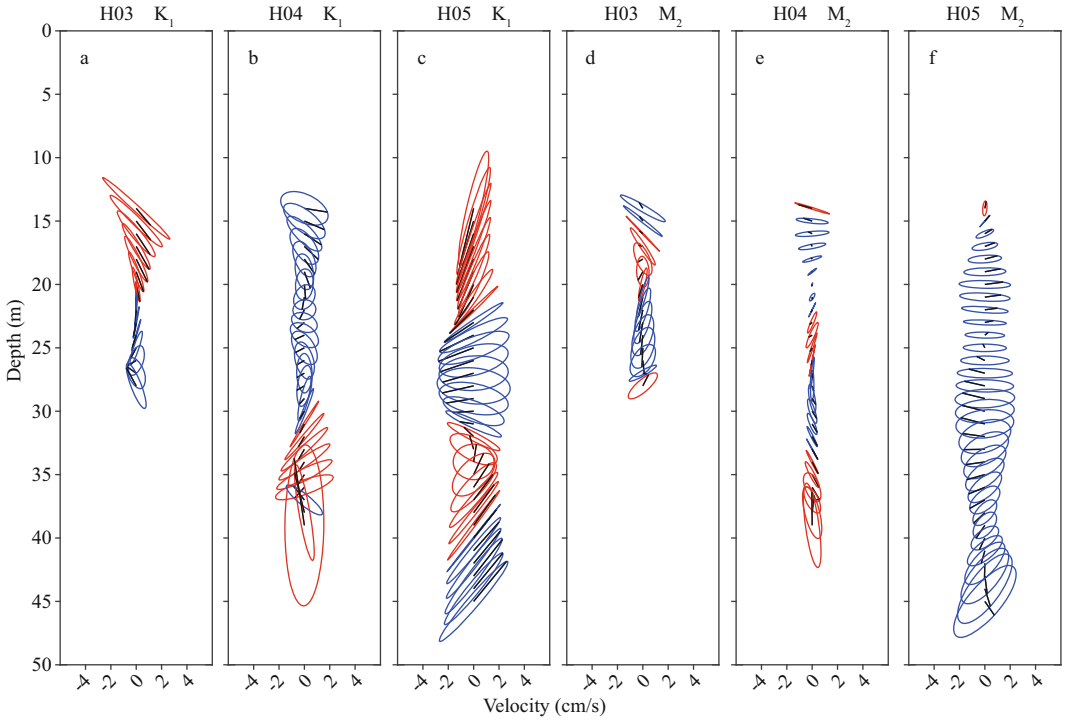

Fig.7 Baroclinic tidal ellipses of K_1 (a–c) and M_2 (d–f) constituents at H03–05

Blue and red colors denote the velocity vectors rotating anticlockwise and clockwise, respectively. The black line in the ellipses shows the velocity vector at 15:58 (local time), which is the time of the first sample at H03.

that the baroclinic K_1 tide is dominated by first-mode structure while the M_2 tide presents a higher modal structure with prominent second-mode motions, using two-month (July–September) moored observations (the water depth is ~114 m) on the shelf of northwestern South China Sea east of Wenchang, which is consistent with the modal structure at H05. The transition depths at H05 are shallower than those in Xu et al. (2011) in which the transition depth of the first-mode K_1 tide is 45 m and those of the high-mode M_2 tide are around 35 m and 70 m. The difference of the transition depths is however understandable with regard for the different bottom depth at the two sites and the possible effect from nonlinear bottom drag (Xu et al., 2011), which can also be speculated from the deepening of the transition depth of K_1 tide from 20 m at H03–04 to 33 m at H05. Except for that, the different stratification and background current at two sites in different seasons, which are generally regarded to influence the propagation of baroclinic tide, are also possible factors that affect the structure of the baroclinic tide (Xu et al., 2013). At H04, the amplitudes of the K_1 and M_2 tides vary similarly from shallow to deep, although the K_1 tide is stronger than the M_2 tide. At H05, K_1 is mainly in the N-S direction above 22 m and below 35 m and in the E-W direction in the middle layer. The M_2 tide is slightly weak relative to the K_1 tide, with a nearly E-W direction at 16–35 m. The rotations of the velocity vectors for the two constituents show an interchange between the clockwise and anticlockwise rotations with depth, except for the constancy of the anticlockwise rotation for the M_2 tide at H05.

At the MR site, all the four tidal constituents exhibited high-mode structures for the duration of early-January to early-March, 2015 (Fig.8). The O_1 tide is the dominant constituent with a maximum velocity of approximately 1.5 cm/s, although it is rather weak compared to the barotropic O_1 tide (refer to Table 1). The K_1 and M_2 tides (mostly less than 1 cm/s) are both weaker than the O_1 tide, but they have strong amplitudes (~1 cm/s) at the surface layer. The velocity vectors of the O_1 tide rotate mostly clockwise, while other tidal constituents exhibit rotation in varying directions.

The baroclinic K_1 and M_2 tidal energies during the observation in February 2012 exhibit a vertically propagating feature in both the cross-shore and along-shore directions (Fig.9) where there is evidence of different vertically propagating directions at various depth layers. This feature is consistent with the vertical variation of the phase in Fig.10, which denotes the delay of the tide with depth. The increasing (decreasing) phase with depth refers to the downward (upward) propagation of the phase, implying an

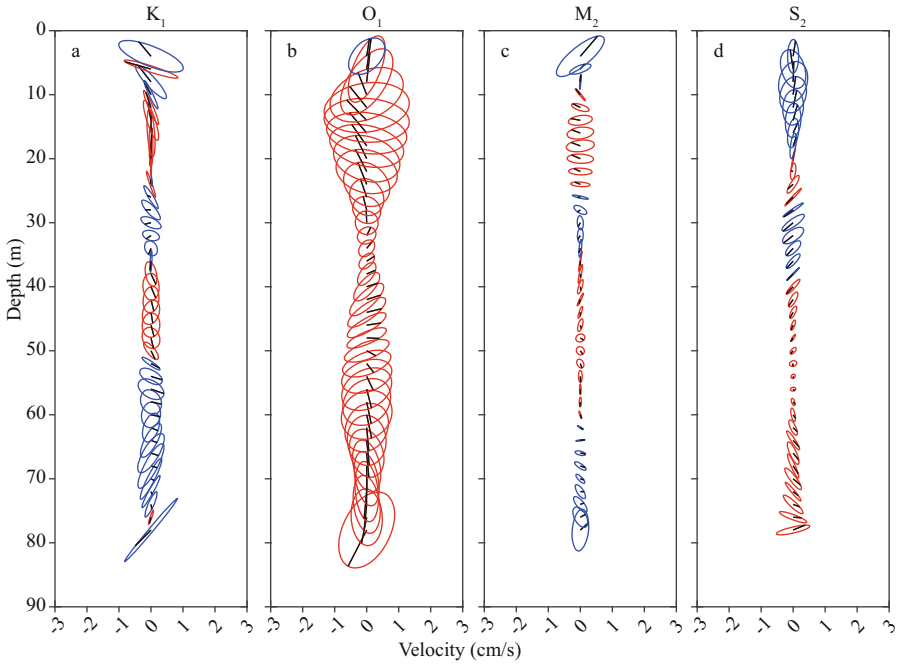

Fig.8 Baroclinic tidal ellipses of four major constituents at the MR site

The colors and black lines are the same as in Fig.7.

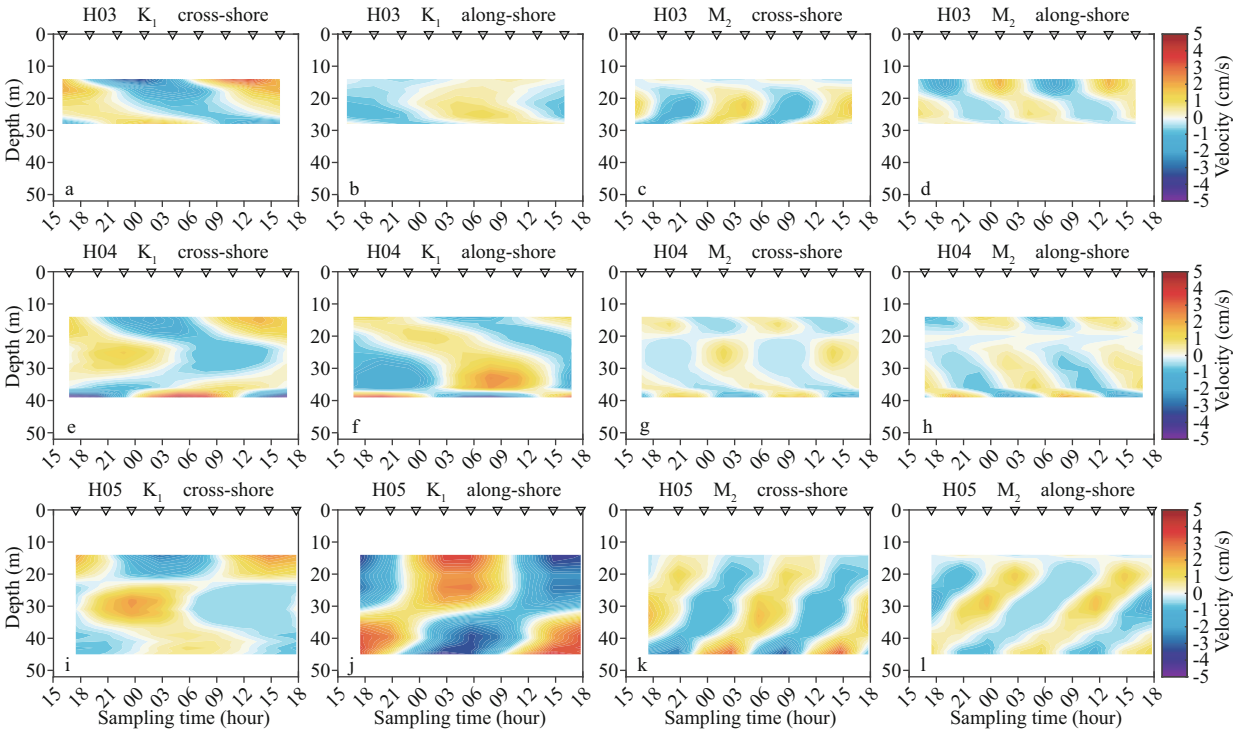

Fig.9 Cross-shore and along-shore velocities for the baroclinic K_1 and M_2 tides at H03–05

Each row shows the result at one station (H03, H04, and H05 from top to bottom). The triangles denote the sampling time.

upward (downward) energy propagation of the internal tide. The K_1 tide at H03 reveals a downward-propagating phase and upward-propagating energy (Fig.10), which is consistent with the distribution of the cross-shore velocity of the K_1 tide (Fig.9). This implies that the cross-shore component is dominant in the K_1 baroclinic tidal energy, which can be seen at H04 as well, except for the transition below 37 m. The phase of the M_2 tide at H03 increased in the upper layer and decreased in the lower layer (Fig.10), which is identical to the propagation feature of the cross-shore velocity (Fig.9). At H04, the phase propagation

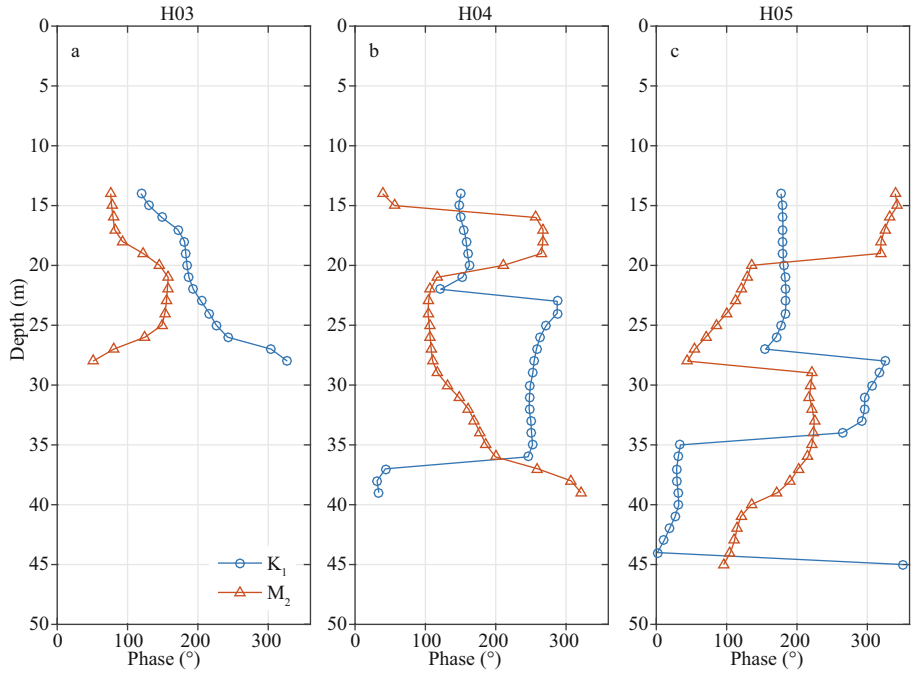

Fig.10 Variation of phase with depth at H03–05

The blue and red curves denote the K_1 and M_2 components, respectively.

of the M_2 tide varies with depth and is likely related to both the cross-shore and along-shore velocities owing to similar variations in the two directions. The vertical structures of the velocities are also similar at H05, and the phase shows a consistent feature of upward propagation.

3.3.2 Effect of tidal current on isopycnal fluctuation

The depth of the isopycnals (Fig.11a–c) revealed periodic features similar to those of the isotherm fluctuations (Fig.2a–c) during the observation in February 2012 with vertically opposite variations especially at H05, which probably results from the tidal motions. To further investigate the effects of diurnal and semidiurnal tides, the time series of isopycnal fluctuations was decomposed. Similar to the decomposition of the current in Section 2.3, the isopycnal fluctuations can be decomposed into diurnal (Fig.11d–f), semidiurnal (Fig.11g–i), and residual components using the least-square method. Both the diurnal and semidiurnal isopycnal fluctuations reach O(5 m) at H03, O(8 m) at H04, and O(10 m) at H05. The isopycnal fluctuations exhibit little vertical variation, as the barotropic signals dominate, supposedly resulting from barotropic tidal motions. Furthermore, the tidal effects weaken from the relatively deep H05 station to the shallow H03. The signals with a K_1 period are stronger than those with an M_2 period at H03 and H05. However, the effect on the fluctuation from the M_2 tide was dominant at H04.

3.3.3 Energy flux of internal tide

3.3.3.1 Method to calculate energy flux

According to Nash et al. (2004), the horizontal energy flux of the internal tide (or the aforementioned baroclinic tide), F_E, can be obtained from the product of the wave-induced pressure anomaly p' and baroclinic velocity anomaly $V'=(u', v')$, which is

$$F_E=<p'V'>_{\phi}, \tag{5}$$

and $<>_{\phi}$ denotes the mean value over one wave period here.

The pressure anomaly is obtained using the hydrostatic equation

$$p'(z,t)=p_{\mathrm{surf}}(t)+\int_{z}^{0}\rho'(\hat{z},t)g\mathrm{d}\hat{z}, \tag{6}$$

in which $p_{\mathrm{surf}}(t)$ denotes the surface pressure and ρ' denotes the density anomaly. The first item in the right-hand side of Eq.6, the surface pressure $p_{\mathrm{surf}}(t)$, can be deduced from the baroclinicity condition

$$\frac{1}{H}\int_{-H}^{0}p'(z,t)\mathrm{d}z=0. \tag{7}$$

Using Eqs.6 & 7, the surface pressure can be obtained from the integral of the density anomaly ρ', which is

$$p_{\mathrm{surf}}(t)=-\frac{1}{H}\int_{-H}^{0}\int_{z}^{0}\rho'(\hat{z},t)g\mathrm{d}\hat{z}\mathrm{d}z. \tag{8}$$

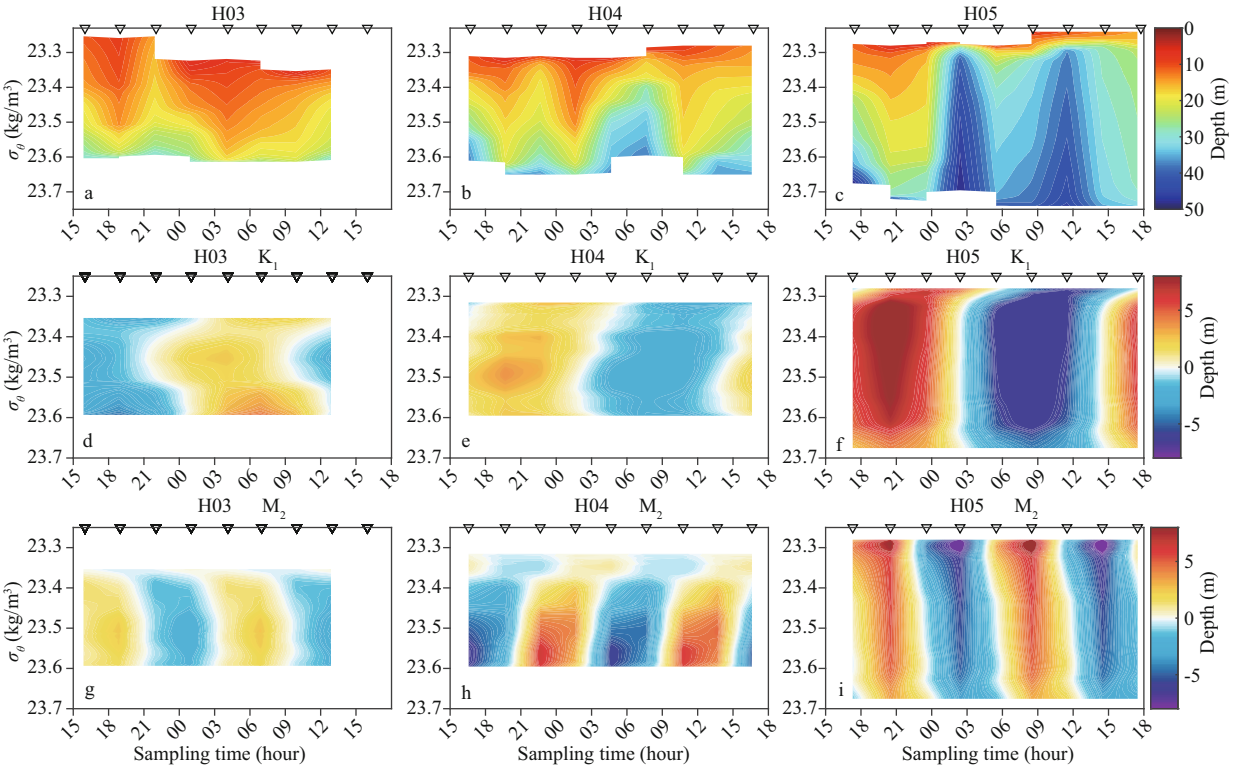

Fig.11 Depth of isopycnals (a–c) and decomposition of isopycnal displacement in the K_1 (d–f) and M_2 (g–i) periods at H03–05

The triangles denote the sample time.

Combining Eqs.6 & 8 leads to

$$p'(z,t)=-\frac{1}{H}\int_{-H}^{0}\int_{z}^{0}\rho'(\hat{z},t)g\mathrm{d}\hat{z}\mathrm{d}z+\int_{z}^{0}\rho'(\hat{z},t)g\mathrm{d}\hat{z}, \quad (9)$$

from which one sees that the density anomaly ρ' needs to be computed first. To perform this,

$$\rho'(z,t)=\frac{\langle\rho(z,t)\rangle}{g}\langle N^2\rangle\xi(z,t), \quad (10)$$

is used, in which $\langle\rho(z,t)\rangle$ is the time-averaging density profile, $\langle N^2\rangle$ is the time-averaging buoyancy frequency and $\xi(z,t)$ is the vertical displacement of isopycnal. Combining Eqs.9 & 10, the pressure anomaly can be obtained from

$$p'(z,t)=-\frac{\langle\rho(z,t)\rangle}{H}\int_{-H}^{0}\int_{z}^{0}\langle N^2\rangle\xi(\hat{z},t)\mathrm{d}\hat{z}\mathrm{d}z+\langle\rho(z,t)\rangle\int_{z}^{0}\langle N^2\rangle\xi(\hat{z},t)\mathrm{d}\hat{z}. \quad (11)$$

The velocity anomaly is computed using

$$V'(z,t)=V(z,t)-\langle V(z,t)\rangle-\overline{V}(t), \quad (12)$$

where $V(z,t)$ is the velocity of the baroclinic current for each tidal constituent (K_1 or M_2), which is obtained in Section 2.3. $\overline{V}(t)$ and $\langle V(z,t)\rangle$ are the depth-averaged velocity and the time-averaged velocity, respectively. Then, combining Eq.11 and Eq.12, the energy flux of the internal tide can be calculated using Eq.5.

3.3.3.2 Energy flux of internal tide

The energy fluxes of the K_1 and M_2 internal tides were obtained at the three stations based on successive observations in February 2012 (Figs.12–14). The period of the flux is half that of the tidal constituents, which is consistent with the implication derived from the definition of the energy flux. The time series of both the along-shore and cross-shore components reveals the vertically propagating features of the baroclinic tidal phase and energy. The K_1 tide has a two-layer structure in both the cross-shore and along-shore directions at H03, whereas the M_2 tide has a three-layer structure. The transition depth of the two-layer K_1 tide and middle layer with the weak energy flux of the M_2 tide are both approximately 20 m, which is consistent with the shift in depth of the first-mode baroclinic tidal current (Fig.7). The energy flux of the M_2 tide varies regularly, while that of the K_1 tide reveals a downward phase-propagation signal, which requires further investigation. Both the K_1 and M_2 tides have intense offshore energy propagation in the upper layer of H03. However, the depth-integrated energy flux over one period is -0.013 W/m onshore for the K_1 tide and 0.076 W/m offshore for the M_2

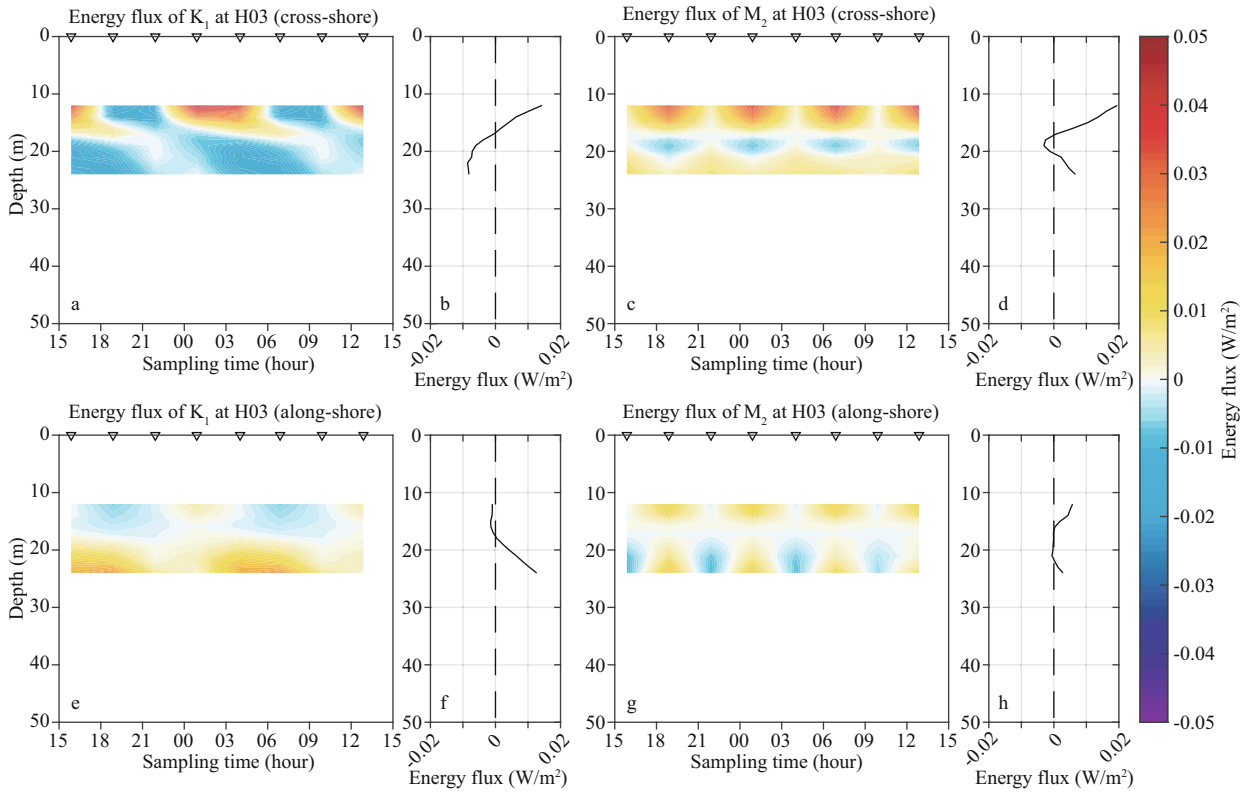

Fig.12 Energy flux variation of baroclinic K_1 (a, e) and M_2 (c, g) tidal constituents at H03, and the corresponding mean energy flux profile over one period (b, d, f, h)

The upper/lower panels are the fluxes in the cross-shore/along-shore direction.

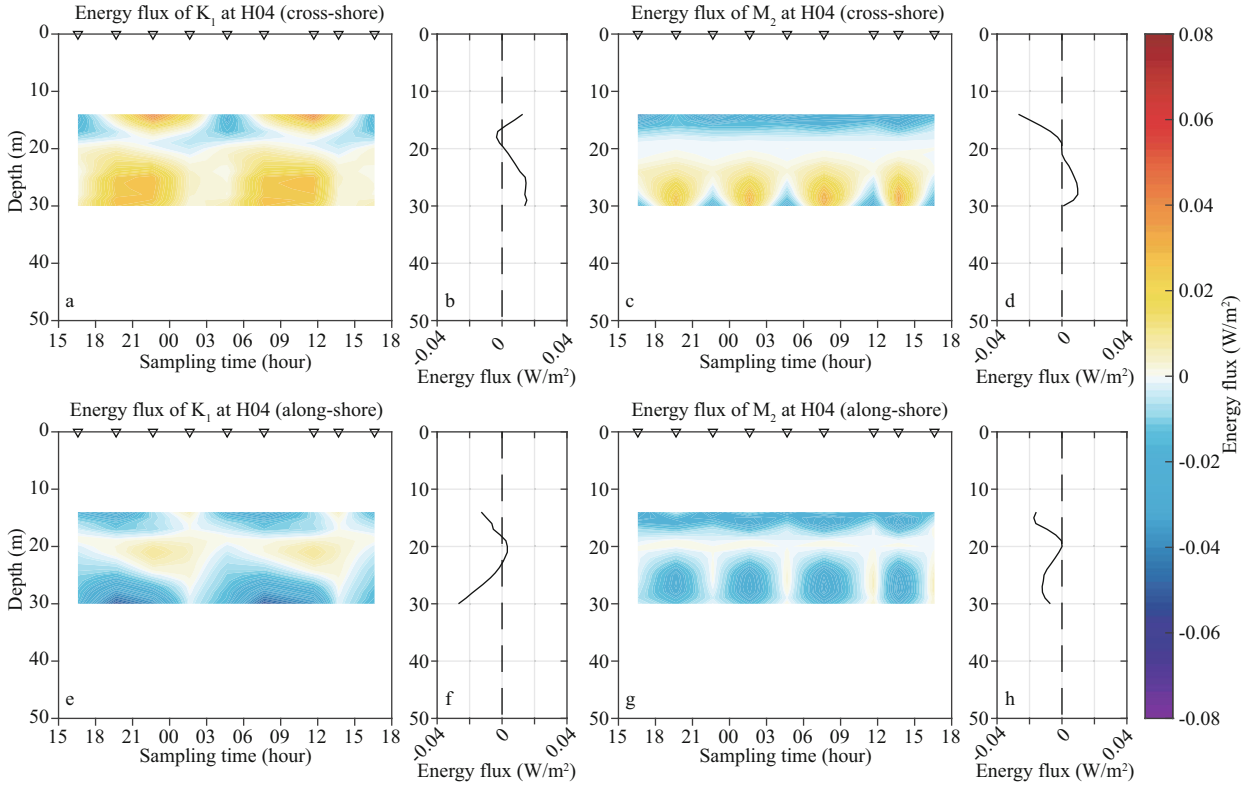

Fig.13 Same as Fig.12 but for H04

The ranges of the *x*-axis in (b, d, f, h) and color scale are both larger than those of Fig.12.

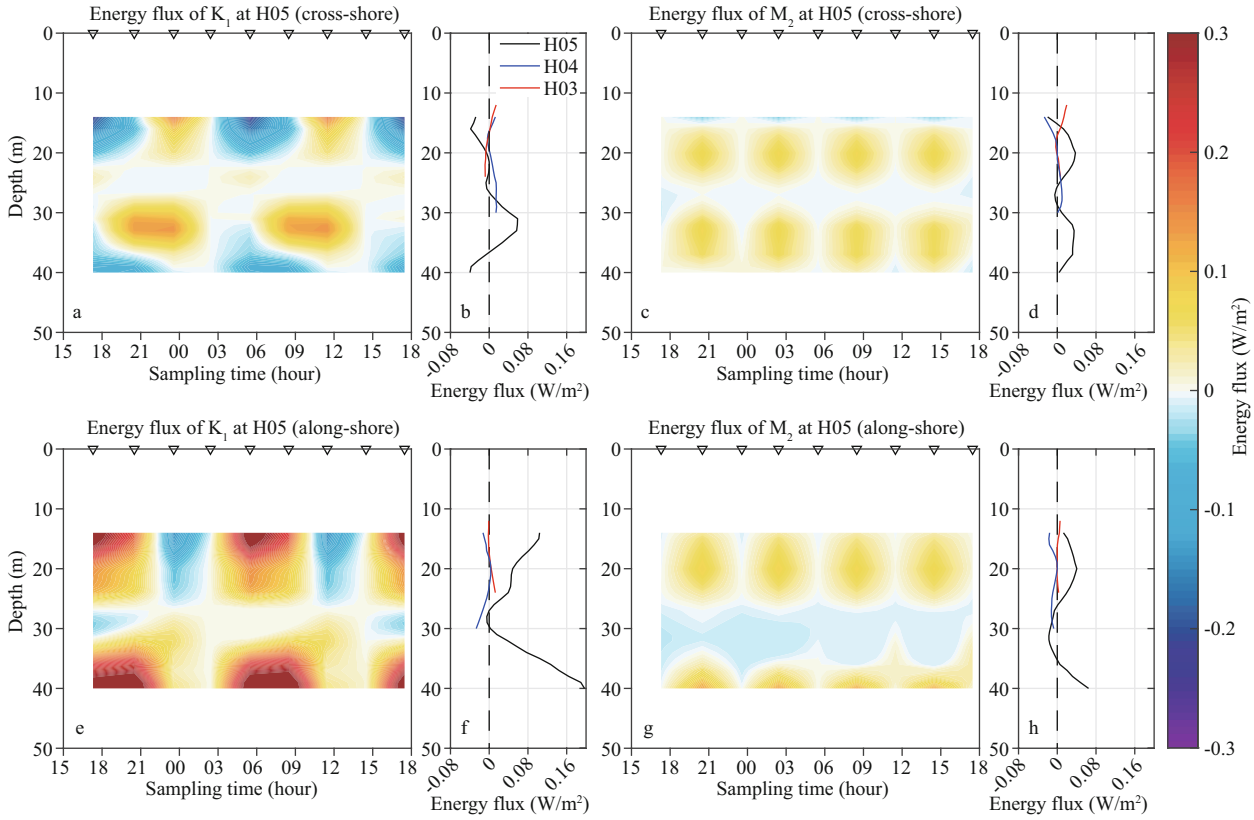

Fig.14 Same as Fig.12 but for H05

The extra blue and red curves in (b, d, f, h) denote the mean energy flux profiles at H04 and H03 shown in Fig.13b, d, f, h and Fig.12b, d, f, h, respectively. The ranges of the *x*-axis in (b, d, f, h) and color scale are both larger than those of Figs.12 and 13.

tide. In the along-shore direction, the net energy fluxes for both tidal components are northeastward.

The energy flux at H04 is more intense than that at H03 (note the different scales at the right, Fig.13), with a three-layer structure and a minimum energy flux at 20 m for both the K_1 and M_2 tides. The depth of the minimum flux was close to the transition depth of the baroclinic tidal modes (Fig.7). The depth-integrated energy flux over one period is 0.134 W/m offshore for the K_1 tide and -0.014 W/m onshore for the M_2 tide. The net fluxes of the two tidal constituents are both southwestward owing to the strong negative values at most depths in the along-shore direction.

At H05, the energy fluxes of both the K_1 and M_2 tides are the strongest of the three stations, with multilayer structures (Fig.14). Note that the maximum of the scales at the right is 0.3 W/m. The energy flux of the K_1 tide becomes stronger than that of the M_2 tide at this station, unlike the comparable feature at the other two stations. The energy flux of the K_1 tide has a stronger component in the along-shore direction than that in the cross-shore direction, with a depth-integrated northeastward net flux. The depth-integrated cross-shore flux of the K_1 tide over one period is 0.052 W/m offshore, with a complex vertical structure. The M_2 tidal energy flux is still regularly periodic, similar to that at the other stations, and the mean flux is nearly positive at all depths, suggesting a net offshore propagation. The mean flux is mainly positive in the along-shore direction, except for the weakly negative flux at 27–35 m, implying a net northeastward flux. The depth-integrated flux of the M_2 tide over one period is 0.471 W/m offshore. Comparing with the energy flux at H04 and H03 (blue and red curves in Fig.14b, d, f, h), one sees that the energy flux of both K_1 and M_2 tide decreased significantly from H05 to H04 above 30 m (the variation below 30 m is unclear because of lacking data at H04), especially for that of the K_1 tide in the alongshore direction. The energy fluxes at H04 and H03 are close with a slight decrease from H04 to H03. Yan (2015) showed the TPXO simulated barotropic tidal energy flux of four primary constituents in the northern SCS and revealed that a significant portion of the tidal energy propagated westward along the continental slope from the Luzon Strait, a fraction of which veered northwestward towards the east of Hainan Island, where there is an non-negligible

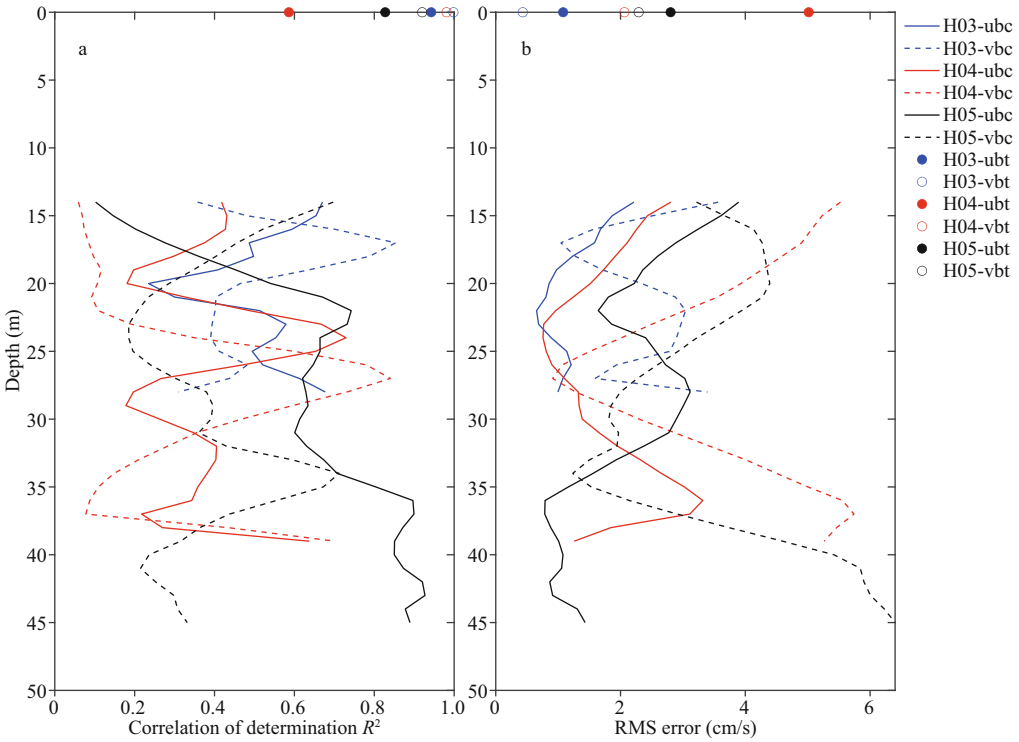

Fig.15 Correlation of determination (a) and root mean square (b) of the error for the barotropic and baroclinic currents at H03-05

The "ubc", "vbc", "ubt", and "vbt" denote the zonal baroclinic current, meridional baroclinic currnet, zonal barotropic current, and meridional barotropic current, respectively.

barotropic to baroclinic conversion rate. Regarding the variation in energy flux at the three stations, the prominent decrease in energy flux from H05 to H03 suggests the possible propagation of energy from the offshore to the inshore and possible dissipation due to bottom friction (Gao, 2013; Yan, 2015).

4 DISCUSSION

4.1 Tidal decomposition method

Regarding the effectiveness of the method to estimate the tidal current for the 25-h time series in this study, the least-square method used here is a traditional tidal current analysis method and has been widely and successfully used to derive tidal currents from length-limited observations (Emery and Thomson, 1998; Tian et al., 2006; Byun and Hart, 2018). It revealed a performance similar to that of the results using the T-Tide toolbox. We further calculated the kinetic energy of the estimated barotropic current composed of the K_1 tide and M_2 tide, with the results revealing that they occupy 98% of the kinetic energy of the raw barotropic current, suggesting that the method is effective in grasping the primary signal.

Furthermore, the correlation of determination R^2, and the root mean square (RMS) of the error between the estimated velocity and the observed time series, are checked to evaluate the tidal estimation (Fig.15). The correlation of determination R^2, which is defined as the ratio of variance explained to total variance, can measure the goodness of fit of the least-square regression curve (Emery and Thomson, 1998). R^2 is large if the regression is good and vice versa.

It can be seen that for the barotropic current (dots in Fig.15), R^2 mostly exceeds 0.8 and the RMS errors are below 3 cm/s, except for R^2 around 0.6 and RMS error around 5 cm/s for the zonal velocity at H04 (solid red dots). The results indicate the goodness of fit and low errors. It is therefore regarded that the tidal analysis for the barotropic current is reliable.

For the baroclinic current (lines in Fig.15), R^2 are generally larger than 0.4 with higher values over 0.7 at depths of vertical mode cores, while low values about 0.2 at depths of mode reversal (Figs.4 & 9). The RMS errors are also mainly lower than 3 cm/s, which is smaller than the amplitudes of the tidal current and the raw current. Some high values over 4 cm/s at the top and bottom layers are probably affected by the shallow water constituents, which are not resolved from coarse sampling but smaller compared to the diurnal and semidiurnal components. Though R^2 and the RMS error of the baroclinic current is respectively

a little lower and larger than that of the barotropic current, the results of the barotropic current are still reliable especially in the core layers of the vertical modes. Moreover, the barotropical currents occupy more than 63% of the total current and are stronger than the baroclininic currents. The tidal analysis here catches the primary features of the observations.

4.2 Tidal components and spring-neap condition

For the tidal component, the K_1 and M_2 tides were used as proxies for diurnal and semidiurnal tides at the successive stations because of the limited sampling frequency. The choice is reasonable because the two components are dominant, as shown in previous studies (Fang, 1986). We checked different pairs of tides (one diurnal tide and one semidiurnal tide) from four primary components (K_1, O_1, M_2, and S_2); similar results were derived qualitatively and quantitatively, suggesting that the effect of the selection of tide components is negligible. Analysis on a 64-h moored time series at H03 (unpublished data) revealed the dominance of the K_1 tide and M_2 tide.

Using the time series of the tide level at Port of Bo'ao from the National Marine Data Information Service (2011), the spring tide occurred on February 7 and February 19 and the neap tide occurred on February 13 and February 25. Suppose that the tide at the successive stations is similar to that at the port, the observation duration (February 23–24) is during the shifting time from spring tide to neap tide. The time series of predicted tidal current near the stations using TPXO model (Egbert and Erofeeva, 2002) is also checked. The spring tide occurred on February 7 and February 20 and the neap tide occurred on February 14 and February 29. Therefore, the results in this research reveal the features of the tidal current near neap tide. Further investigation about the spring-neap cycle is needed based on long-term observations.

4.3 Propagation of the internal tide

There are previous studies showing the long-range westward propagation of the internal K_1 and M_2 tide generated at the Luzon Strait based on satellite observations (Zhao, 2014) and numerical modeling (Xu et al., 2016; Yan et al., 2020), which can propagate across the deep basin and arrive at the western continental slope (though it decreases when propagating to the west and is rather small relative to that in the far east), suggesting that the energy flux of internal tide near the successive stations probably indicates the feature of the internal tide propagated far away from the east. Moreover, Xu et al. (2016) showed remarkable barotropic to baroclinic conversion rate of K_1 tide along the northern continental slope of South China Sea, and Yan et al. (2020) revealed that the slope region around 200-m depth in the southeast of Hainan Island is generation region of baroclinic M_2 tide and the barotropic to baroclinic conversion rate along the slope is significant in winter, suggesting the possible effect from the generated internal tide along the slope on the energy flux and the westward propagation to the study area. However, this issue needs support of more data and is out of this paper's scope and will be investigated in the future.

5 CONCLUSION

The tidal current was analyzed using observations from three successive stations northeast of Hainan Island and a moored time series southeast of the island, for which the least-square method and T-Tide toolbox were applied, respectively, to extract the tidal current. The result captured the primary signal of the time series; the K_1 and M_2 tides were used as proxies of the diurnal and semidiurnal tides, respectively.

The results reveal that the diurnal tidal current (K_1) is comparable to the semidiurnal component (M_2) in the north (4–8 cm/s at H03–05); however, the O_1 tide is dominant (~5 cm/s) and much stronger than the other components (1–2 cm/s) in the south. This leads to an irregular semidiurnal tidal current in the north and an irregular diurnal tidal current in the south. The directions turn from NE-SW at the deeper station (H05) to N-S at the shallower station (H03) for the K_1 tide and from NW-SE to NE-SW for the M_2 tides. The velocity vectors of the K_1 tide rotate clockwise at H03 and H04 and rotate anticlockwise at H05 and the MR site. Meanwhile, the barotropic M_2 tide reveals a clockwise rotation at H03–05 and anticlockwise at the MR site. The O_1 tide is dominant at the MR site with an inclination along the isobaths and a nearly rectilinear feature. The residual current has a significant westward or northwestward component, which is speculated to be a consequence of veered wind forcing during a wind shift event.

The baroclinic K_1 tide exhibited a first-mode structure at three stations, as dose the M_2 tide at H03. Higher-mode features are revealed at H04 and H05 for the M_2 tides. The rotation of velocity vectors varies with depth except for the nearly constant rotation of the M_2 tide at H05 and the O_1 tide at the MR site. The K_1 and M_2 tides have similar intensities

at successive stations, whereas the O_1 tide is clearly dominant at the MR site. The phase and energy of the internal tides reveal a vertically propagating feature, which is shown both in the velocity field and vertical variation of the phase. The result of the decomposition of the isopycnal fluctuation signals shows that the diurnal and semidiurnal isopycnal fluctuations both reach *O*(5 m) at H03, *O*(8 m) at H04, and *O*(10 m) at H05. They also demonstrate little vertical variation, as they are dominated by the barotropic signals, with a prominent K_1 tide signal at H03 and H05 and an M_2 tide signal at H04. The time series of both the along-shore and cross-shore components of the horizontal internal tide energy flux reveal the vertically propagating feature of the phase and energy at the three stations. The energy flux decreases from *O*(0.1 W/m) at H05 to *O*(0.01 W/m) at H03, implying energy propagation from offshore to inshore.

6 DATA AVAILABILITY STATEMENT

The data at successive stations analyzed during the study are available from the corresponding author upon reasonable request. The mooring data at the MR station were downloaded from the "South China Sea and Adjacent Seas Data Center, National Earth System Science Data Center, National Science & Technology Infrastructure of China" (http://ocean.geodata.cn).

7 ACKNOWLEDGMENT

The authors thank editors and three anonymous reviewers for useful and constructive suggestions on the manuscript. We are also grateful to all the people working for the valuable cruise observations east of Hainan Island in winter 2012.

References

Byun D O, Hart D E. 2018. Predicting tidal currents using 25-h observations through a complete tidal species modulation with tidal current constant corrections method. *Journal of Atmospheric and Oceanic Technology*, **35**(12): 2405-2420, https://doi.org/10.1175/JTECH-D-18-0120.1.

Cao D M, Fang G H. 1990. A numerical model for tides and tidal currents in northern South China Sea. *Tropic Oceanology*, **9**(2): 63-70. (in Chinese with English abstract)

Deng X D, Liu J L, Cai S Q. 2013. Analyses of the tidal current characteristics on the continental shelf of the Xisha Islands in the South China Sea. *Journal of Tropical Oceanography*, **32**(4): 8-12, https://doi.org/10.3969/j.issn.1009-5470.2013.04.002. (in Chinese with English abstract)

Ding W L. 1986. Distribution of tides and tidal currents in the South China Sea. *Oceanologia et Limnologia Sinica*, **17**(6): 468-480. (in Chinese with English abstract)

Editorial Board of Marine Atlas. 2006. Marine Atlas of South China Sea: Hydrology. China Ocean Press, Beijing. (in Chinese)

Egbert G D, Erofeeva S Y. 2002. Efficient inverse modeling of barotropic ocean tides. *Journal of Atmospheric and Oceanic Technology*, **19**(2): 183-204, https://doi.org/10.1175/1520-0426(2002)019<0183:EIMOBO>2.0.CO;2.

Egbert G D, Ray R D. 2000. Significant dissipation of tidal energy in the deep ocean inferred from satellite altimeter data. *Nature*, **405**(6788): 775-778, https://doi.org/10.1038/35015531.

Emery W J, Thomson R E. 1998. Data Analysis Methods in Physical Oceanography. Elsevier, Amsterdam. p.643.

Fang G H, Cao D M, Huang Q Z. 1994. Numerical modeling for tides and tidal currents in South China Sea. *Acta Oceanologica Sinica*, **16**(4): 1-12. (in Chinese)

Fang G H, Kwok Y K, Yu K, Zhu Y H. 1999. Numerical simulation of principal tidal constituents in the South China Sea, Gulf of Tonkin and Gulf of Thailand. *Continental Shelf Research*, **19**(7): 845-869, https://doi.org/10.1016/S0278-4343(99)00002-3.

Fang G H. 1986. Tide and tidal current charts for the marginal seas adjacent to China. *Chinese Journal of Oceanology and Limnology*, **4**(1): 1-16, https://doi.org/10.1007/BF02850393.

Gao D L, Jin G Z, Lü X Q. 2017. Temporal variations in internal tide multimodal structure on the continental shelf, South China Sea. *Chinese Journal of Oceanology and Limnology*, **35**(1): 70-78, https://doi.org/10.1007/s00343-016-5168-0.

Gao X M. 2013. Data Assimilation of Tides in the South China Sea Using Adjoint Method Considering the Internal Tide Dissipation. Ocean University of China, Qingdao. (in Chinese)

Gao Y, Huang Y X, Lin H Y, Sun Z Y, Zhu J, Hu J Y. 2020. Surface currents measured by GPS drifters in Daya Bay and along the eastern Guangdong coast. *Frontiers of Earth Science*, **14**(2): 376-383, https://doi.org/10.1007/s11707-019-0776-6.

He Q, Wei Z X, Wang Y G. 2012. Study on the sea currents in the northern shelf and slope of the South China Sea based on the observation. *Acta Oceanologica Sinica*, **34**(1): 17-28. (in Chinese with English abstract)

Hu J Y, Wang X H. 2016. Progress on upwelling studies in the China seas. *Reviews of Geophysics*, **54**(3): 653-673, https://doi.org/10.1002/2015RG000505.

Ke Z M. 2007. The Characters of Internal Waves and Internal Tides in Wenchang. Institute of Oceanology, Chinese Academy of Sciences, Qingdao. (in Chinese)

Munk W, Wunsch C. 1998. Abyssal recipes II: energetics of tidal and wind mixing. *Deep Sea Research Part I: Oceanographic Research Papers*, **45**(12): 1977-2010, https://doi.org/10.1016/S0967-0637(98)00070-3.

Nash J D, Kunze E, Toole J M, Schmitt R W. 2004. Internal tide reflection and turbulent mixing on the continental slope.

Journal of Physical Oceanography, **34**(5): 1117-1134, https://doi.org/10.1175/1520-0485(2004)034<1117:ITRATM>2.0.CO;2.

National Marine Data Information Service. 2011. Tide Tables: Vol. 3: From the Taiwan Straits to the Beibu Gulf. China Ocean Press, Beijing, China. p.1-587. (in Chinese)

Pawlowicz R, Beardsley B, Lentz S. 2002. Classical tidal harmonic analysis including error estimates in MATLAB using T_TIDE. *Computers & Geosciences*, **28**(8): 929-937, https://doi.org/10.1016/S0098-3004(02)00013-4.

Tian J W, Yang Q X, Liang X F, Xie L L, Hu D X, Wang F, Qu T D. 2006. Observation of Luzon strait transport. *Geophysical Research Letters*, **33**(19): L19607, https://doi.org/10.1029/2006GL026272.

Xie L L, Pallàs-Sanz E, Zheng Q A, Zhang S W, Zong X L, Yi X F, Li M M. 2017. Diagnosis of 3D vertical circulation in the upwelling and frontal zones east of Hainan Island, China. *Journal of Physical Oceanography*, **47**(4): 755-774, https://doi.org/10.1175/JPO-D-16-0192.1.

Xie L L, Zhang S W, Zhao H. 2012. Overview of studies on Qiongdong upwelling. *Journal of Tropical Oceanography*, **31**(4): 35-41, https://doi.org/10.11978/j.issn.1009-5470.2012.04.005. (in Chinese with English abstract)

Xu Z H, Liu K, Yin B S, Zhao Z X, Wang Y, Li Q. 2016. Long-range propagation and associated variability of internal tides in the South China Sea. *Journal of Geophysical Research*: *Oceans*, **121**(11): 8268-8286, https://doi.org/10.1002/2016JC012105.

Xu Z H, Yin B S, Hou Y J, Xu Y S. 2013. Variability of internal tides and near-inertial waves on the continental slope of the northwestern South China Sea. *Journal of Geophysical Research*: *Oceans*, **118**(1): 197-211, https://doi.org/10.1029/2012JC008212.

Xu Z H, Yin B S, Hou Y J. 2011. Multimodal structure of the internal tides on the continental shelf of the northwestern South China Sea. *Estuarine*, *Coastal and Shelf Science*, **95**(1): 178-185, https://doi.org/10.1016/j.ecss.2011. 08.026.

Yan T, Jing Z Y, Qi Y Q, Wang D X. 2016. Characteristics of internal tides in deep water northwest of the Xisha Islands. *Chinese Journal of Geophysics*, **59**(7): 2587-2597, https://doi.org/10.6038/cjg20160723. (in Chinese with English abstract)

Yan T, Qi Y Q, Jing Z Y, Cai S Q. 2020. Seasonal and spatial features of barotropic and baroclinic tides in the northwestern South China Sea. *Journal of Geophysical Research*: *Oceans*, **125**(1): e2018JC014860, https://doi.org/10.1029/2018JC014860.

Yan T. 2015. Observations and Numerical Simulations of the Internal Tides in the Northwestern South China Sea. South China Sea Institute of Oceanology, Chinese Academy of Sciences, Guangzhou. (in Chinese)

Yang W K, Yin B S, Yang D Z, Xu Z H. 2013. Application of FVCOM in numerical simulation of tide and tidal currents in the northern South China Sea. *Marine Sciences*, **37**(9): 10-19. (in Chinese with English abstract)

Ye A L, Robinson I S. 1983. Tidal dynamics in the South China Sea. *Geophysical Journal International*, **72**(3): 691-707, https://doi.org/10.1111/j.1365-246X.1983.tb02827.x.

Zhao Z X. 2014. Internal tide radiation from the Luzon Strait. *Journal of Geophysical Research*: *Oceans*, **119**(8): 5434-5448, https://doi.org/10.1002/2014JC010014.

Zhu X H, Ma Y L, Guo X Y, Fan X P, Long Y, Yuan Y C, Xuan J L, Huang D J. 2014. Tidal and residual currents in the Qiongzhou Strait estimated from shipboard ADCP data using a modified tidal harmonic analysis method. *Journal of Geophysical Research*: *Oceans*, **119**(11): 8039-8060, https://doi.org/10.1002/2014JC009855.

Zhu X M. 2009. Numerical Simulations and Studies on the Tides and Tidal Currents in the Marginal Seas Adjacent to China. Ocean University of China, Qingdao. (in Chinese)

Zu T T, Gan J P, Erofeeva S Y. 2008. Numerical study of the tide and tidal dynamics in the South China Sea. *Deep Sea Research Part I*: *Oceanographic Research Papers*, **55**(2): 137-154, https://doi.org/10.1016/j.dsr.2007.10.007.